Research Square

Preprints are preliminary reports that have not undergone peer review.
They should not be considered conclusive, used to inform clinical practice,
or referenced by the media as validated information.

Endothelial RANK signaling triggers bone marrow inflammaging

Yasuhiro Kobayashi

yasuhiro.kobayashi@mdu.ac.jp

Matsumoto Dental University

Rina Iwamoto

Department of Hard Tissue Research, Institute for Oral Science, Matsumoto Dental University

Takumi Takahashi

Department of Hard Tissue Research, Institute for Oral Science, Matsumoto Dental University

Masayoshi Ishida

Department of Hard Tissue Research, Institute for Oral Science, Matsumoto Dental University

Zhifeng He

Department of Hard Tissue Research, Institute for Oral Science, Matsumoto Dental University

Kohei Murakami

Department of Veterinary Immunology, Faculty of Veterinary Medicine, Okayama University of Science

Tomoyo Hara

Department of Hematology, Endocrinology and Metabolism, Graduate School of Biomedical Sciences, Tokushima University

Byambasuren Ganbaatar

Department of Hematology, Endocrinology and Metabolism, Graduate School of Biomedical Sciences, Tokushima University

Hiroki Yamagami

Department of Hematology, Endocrinology and Metabolism, Graduate School of Biomedical Sciences, Tokushima University

Itsuro Endo

Department of Bioregulatory Sciences, Graduate School of Biomedical Sciences, Tokushima University

Takahiro Iguchi

Department of Immunology, Graduate School of Medicine and Faculty of Medicine, The University of Tokyo

Toru Hiraga

Department of Histology and Cell Biology, Matsumoto Dental University

Toshihide Mizoguchi

Tokyo Dental College

Midori Nakamura

Department of Biochemistry, Matsumoto Dental University

Yutaro Ando

Department of Biochemistry, Showa Medical University School of Dentistry

Hisataka Yasuda

Oral Health Science Center, Tokyo Dental College

Masayuki Tsukasaki

Department of Biochemistry, Showa Medical University School of Dentistry

Kazuo Okamoto

Division of Immune Environment Dynamics, Cancer Research Institute, mmune Network Research Unit, Institute for Frontier Science Initiative Kanazawa University

Hiroshi Takayanagi

University of Tokyo

Nobuyuki Udagawa

Department of Hard Tissue Research, Institute for Oral Science, Department of Biochemistry Matsumoto Dental University

---

Article

Keywords:

Posted Date: September 4th, 2026

DOI: https://doi.org/10.21203/rs.3.rs-10285332/v1

License: This work is licensed under a Creative Commons Attribution 4.0 International License. Read Full License

Additional Declarations: There is **NO** Competing Interest.

Endothelial RANK signaling triggers bone marrow inflammaging

Rina Iwamoto[1]†, Takumi Takahashi[1]†, Masayoshi Ishida[1], Zhifeng He[1], Kohei Murakami[2], Tomoyo Hara[3], Byambasuren Ganbaatar[3], Hiroki Yamagami[3], Itsuro Endo[4], Takahiro Iguchi[5], Toru Hiraga[6], Toshihide Mizoguchi[7], Midori Nakamura[8], Yutaro Ando[9], Hisataka Yasuda[7, 8, 9], Masayuki Tsukasaki[9], Kazuo Okamoto [10, 11], Hiroshi Takayanagi[5], Nobuyuki Udagawa[1, 8], Yasuhiro Kobayashi[1]*

1. Department of Hard Tissue Research, Institute for Oral Science, Matsumoto Dental University, Shiojiri, Japan

2. Department of Veterinary Immunology, Faculty of Veterinary Medicine, Okayama University of Science, Imabari, Japan

3. Department of Hematology, Endocrinology and Metabolism, Graduate School of Biomedical Sciences, Tokushima University, Tokushima, Japan

4. Department of Bioregulatory Sciences, Graduate School of Biomedical Sciences, Tokushima University, Tokushima, Japan

5. Department of Immunology, Graduate School of Medicine and Faculty of Medicine, The University of Tokyo, Tokyo, Japan.

6. Department of Histology and Cell Biology, Matsumoto Dental University, Shiojiri, Japan

20 7. Oral Health Science Center, Tokyo Dental College, Tokyo, Japan.

21 8. Department of Biochemistry, Matsumoto Dental University, Shiojiri, Japan.

22 9. Department of Biochemistry, Showa Medical University School of Dentistry, Tokyo, Japan.

23 10. Division of Immune Environment Dynamics, Cancer Research Institute, Kanazawa

24 University, Kanazawa, Japan

25 11. Immune Network Research Unit, Institute for Frontier Science Initiative, Kanazawa

26 University, Kanazawa, Japan

27

28 †These authors contributed equally to this work.

29 *Corresponding author

30 E-mail address: yasuhiro.kobayashi@mdu.ac.jp

31 29 1780 Hiro-oka Gobara, Shiojiri, Nagano 399-0781, Japan

32 30 Tel: +81-263-51-2238, Fax: +81-263-51-2223

33

Abstract

Senescent cell accumulation in the bone marrow promotes inflammaging, hematopoietic stem cell dysfunction, and myeloid-biased hematopoiesis, contributing to the onset of age-related diseases. However, the mechanisms underlying the emergence of senescent cells in the bone marrow remain poorly understood. Here, we identify endothelial RANK signaling as a key regulator of bone marrow senescence. Young *Tnfrsf11b* (osteoprotegerin, OPG)-deficient mice exhibited premature accumulation of senescent cells and myeloid-biased hematopoiesis, phenocopying middle-aged wild-type mice. Endothelial-specific deletion of *Tnfrsf11a* (RANK), blockade of RANKL, and in vivo tracing with fluorescent-labelled RANKL revealed that RANK signaling in endothelial cells drives senescent cell accumulation in the bone marrow. Bulk and single-cell RNA sequencing, and IL-1β neutralization demonstrate that RANK signaling induces IL-1β expression in endothelial cells, which in turn promotes bone marrow inflammaging. These findings identify endothelial RANK as a critical initiator of bone marrow senescence, thereby driving inflammaging, a potential therapeutic target for age-related diseases.

Aging is a major contributor to the onset and progression of various chronic diseases, including type II diabetes mellitus (DM), osteoporosis, sarcopenia[1, 2], particularly in individuals over middle age[3]. In this context, senescent cells have emerged as a potential therapeutic target for age-associated chronic conditions[4, 5]. In vitro studies have demonstrated that cellular senescence can be triggered by DNA damage resulting from various stresses[6-8]. However, the upstream signals that initiate cellular senescence during physiological aging in vivo remain largely undefined.

Senescent cells are characterized by a permanent arrest of the cell cycle, yet they remain metabolically active and secrete a variety of pro-inflammatory cytokines and proteolytic enzymes collectively referred to as the senescence-associated secretory phenotype (SASP)[7]. Through this secretory profile, senescent cells contribute to a persistent, low-grade inflammatory state in tissues—a phenomenon termed “inflammaging”[9]. Accumulating evidence indicates that clearance of senescent cells can ameliorate age-associated organ dysfunction, including in bone tissue[10] and various senolytic therapies are currently being evaluated in clinical trials[11]. A central question in gerontology and age-related disease prevention is how senescent cells arise within tissues. However, the mechanisms underlying the emergence of senescent cells within the bone marrow remain largely unknown.

Receptor activator of NF-κB ligand (RANKL, encoded by *Tnfsf11*), its receptor RANK (encoded by *Tnfrsf11a*), and the decoy receptor osteoprotegerin (OPG, encoded by *Tnfrsf11b*)

69 are known to play crucial roles not only in bone metabolism but also in the development of the
70 immune system in the thymus, lymph nodes, gut, skin, and central nervous system[12]. In
71 addition, they are involved in mammary gland development, regulation of thermogenesis via the
72 brain, and control of the hair cycle[13]. Beyond their physiological functions, RANKL-RANK-
73 OPG signaling has also been implicated in various pathological conditions, including breast
74 cancer progression and metastasis, type 2 DM, and sarcopenia[12, 13]. Interestingly, young OPG-
75 deficient (OPG KO) mice exhibit several phenotypes that resemble those observed in aged
76 animals, such as increased bone marrow adiposity, impaired spermatogenesis, vascular
77 calcification, premature growth plate closure, and severe osteopenia. These findings suggest that
78 excessive or unregulated RANKL-RANK signaling may contribute to the acceleration of aging-
79 related changes. However, the precise mechanisms by which RANKL-RANK signaling
80 promotes aging remain to be elucidated.
81 It has been proposed that continuous low-grade IL-1 signals contribute to the impairment of
82 hematopoietic stem cell function, and then act as a driver of clonal hematopoiesis of
83 indeterminate potential and myeloproliferative and myelodysplastic neoplasm[14]. Moreover, IL-1
84 secreted from bone marrow stromal cells (BMSCs) and macrophages exacerbates hematopoietic
85 aging and platelet-biased hematopoiesis, respectively, in aged mice[15, 16]. Thus, IL-1 signals are
86 largely involved in hematopoietic disorders in aged human and mice. However, which cells

express IL-1, and which cells receive IL-1 in middle-aged bone marrow are not fully understood.

Here, we found that treatment of OPG KO mice with anti-RANKL antibodies rescued age-associated bone phenotypes, including senescent cell accumulation and myeloid-biased hematopoiesis. Fluorescent-labeled RANKL tracing and genetic studies revealed that RANKL-RANK signaling in endothelial cells upregulates IL-1β expression in the bone marrow, thereby inducing cellular senescence in BMSCs and driving myeloid-biased hematopoiesis. Together, these findings identify endothelial RANK signaling as a potential therapeutic target for preventing bone marrow inflammaging.

Results

OPG deficiency accelerates age-associated phenotypes in bone marrow

Both young (8-week-old) and middle-aged (32-week-old) OPG KO exhibited lower bone mass with higher bone marrow adiposity, mirroring characteristics commonly observed in middle-aged and elderly humans (Extended Data Fig. 1a, b) as shown previously[17]. This prompted us to investigate additional age-associated phenotypes such as the accumulation of senescent cells, myeloid-biased hematopoiesis, and inflammaging[18, 19], in OPG KO mice. SPiDER-β-gal (fluorescent substrate for senescence-associated-β-galactosidase)-positive senescent cells were increased in young and middle-aged OPG KO as well as middle-aged wild-type mice (Fig. 1a) associated with the significant decreasing Ki67-positive proliferative cells and the increased perilipin-positive adipocytes and CD41a-positive megakaryocytes (Extended Data Fig. 1b-d), as previously shown in aged bone marrow[20]. Consistent with the myeloid-biased hematopoiesis observed in aged humans and mice[21, 22], young OPG KO mice exhibited increased neutrophil and reduced lymphocyte frequencies, a phenotype also observed in middle-aged WT and OPG KO mice (Fig. 1b). These findings suggest that myeloid-biased hematopoiesis is already established in young OPG KO mice. Furthermore, qRT-PCR analysis revealed upregulation of senescence markers such as *p16* and *p21* and SASP-related genes in bone tissues of OPG KO mice (Fig. 1c).

We next investigated whether the neutralization of RANKL rescues age-related phenotypes in OPG KO mice by the administration of anti-mouse RANKL antibody (anti-RANKL Ab). Anti-RANKL Ab rescued the increased number of SPiDER-β-gal-positive senescent cells, and myeloid-biased hematopoiesis observed in OPG KO mice as well as the decreased bone mass (Fig. 1d-f). Anti-RANKL Ab also decreased the expression of *p16* and *p21* mRNA, increased Ki67-positive cells, and decreased megakaryocytes, but not adipocyte number, in the bone marrow from OPG KO mice (Extended Data Fig. 1e-h).

Endothelial cells are targets of RANKL in middle-aged bone marrow

To determine the RANK-expressing cells in middle-aged bone marrow, fluorescent-labeled recombinant RANKL (Fluor555-rRANKL) was intravenously injected into young and middle-aged mice. Fluor555-rRANKL-positive signals were observed in CD31- or Endomucin (Emcn)-positive endothelial cells from middle-aged bone marrow, but not in young mice (Fig. 2a). Flow cytometric analysis confirmed that Fluor555-rRANKL signals were markedly detected in endothelial cells, but not in BMSC-enriched or CD45-positive immune cell fraction (Fig. 2b).

Immunofluorescence analyses using VE-cadherin (Cdh5)-Cre; tdTomato (VE-cadherin-tom) and RANK-Cre; tdTomato (RANK-tom) reporter mice demonstrated increased numbers and frequencies of VE-cadherin/RANK double-positive cells in middle-aged bone marrow, as well as those of RANK-tom-positive $CD31^{+}Emcn^{+}$ endothelial cells (Fig. 2c,d). In contrast, RANK-

tom-positive cells lacked expression of the leptin receptor (Lepr) and the macrophage marker F4/80 around the bone marrow sinusoid (Extended Data Fig. 2a). Moreover, RANKL-positive areas, including both cellular and extracellular matrix-associated signals, were significantly increased in middle-aged bone marrow (Extended Data Fig. 2b).

Endothelial RANK accelerates age-associated phenotypes in bone

To investigate the role of endothelial RANK signaling in age-related bone phenotypes, we generated endothelial cell-specific RANK-deficient mice (VE-Cadherin-Cre; *RANK*$^{fl/fl}$; EC-RANK cKO). Intravenous fluor555-rRANKL injection confirmed reduced RANK expression in endothelial cells (Extended Data Fig. 3a). μCT analysis showed significantly increased trabecular bone volume, thickness, and number in middle-aged EC-RANK cKO mice versus WTs (Fig. 3a). Histomorphometry revealed increased osteoblast number, osterix-positive osteoblasts, and bone formation rate, while osteoclast number was unchanged (Extended Data Fig. 3b–e), indicating preserved bone mass through enhanced bone formation. Histological and FACS analyses showed fewer p16- and SPiDER-β-gal-positive senescent cells in EC-RANK cKO mice (Fig. 3b, Extended Data Fig. 4a,b). In addition, myeloid-biased hematopoiesis, reduced Ki67-positive cells, increased megakaryocytes, and elevated SASP factors (*Il1b*, *Tnfa*) were rescued (Fig. 3c, Extended Data Fig. 4c–e), suggesting that endothelial RANK signaling drives age-associated bone phenotypes.

153 Impaired hematopoietic recovery has been reported in aged mice after myeloablative 5-
154 fluorouracil (FU) treatment, which also induces fatty marrow formation[15,23]. We therefore
155 examined hematopoietic recovery in middle-aged EC-RANK cKO mice. Histology showed
156 reduced bone marrow cellularity in all groups at day 7 after 5-FU treatment, followed by
157 recovery by day 14 (Extended Data Fig. 4f). Although marrow cellularity during recovery was
158 similar among groups, myeloid-biased hematopoiesis was rescued in middle-aged EC-RANK
159 cKO mice, but not in middle-aged WTs (Fig. 3d,e). These findings suggest that age-associated
160 myeloid-biased hematopoiesis is partly driven by alterations in the bone marrow
161 microenvironment, including endothelial, stromal, and hematopoietic cells.
162 Bone regenerative capacity declines with age[24]. μCT analysis demonstrated that newly
163 formed trabecular bone volume was significantly increased in middle-aged EC-RANK cKO
164 mice (Fig. 3f). Consistently, histological analysis revealed a greater abundance of osterix-
165 positive osteoblasts along newly formed bone surfaces in these mice (Fig. 3g).
166
167 **RANK signaling induces inflammaging through IL-1β**
168 We next performed RNA-seq analysis to identify secreted factors mediating bone marrow
169 senescence downstream of endothelial RANK signaling (Fig. 4a–f). The top 30 genes
170 upregulated in the femora of middle-aged controls (Mcont) relative to young controls (Ycont)
171 predominantly reflected immune and inflammatory responses, proteolysis and cell adhesion,

whereas the top 30 downregulated genes were mainly involved in development and bone formation (Fig. 4a). Comparison with middle-aged EC-RANK cKO mice (McKO) identified 8 downregulated and 3 upregulated genes (Fig. 4b). Among genes elevated in Mcont but reduced in McKO, *Il1b* emerged as a candidate driver of bone marrow senescence, whereas *Col14a1* may act suppressively (Fig. 4c,d).

To validate this, we reanalyzed a public bone marrow scRNA-seq dataset (GSE145477)[25]. UMAP analysis identified four clusters, including a CD31- or Emcn-positive endothelial cluster (Extended Data Fig. 5a). Differential expression and gene ontology analyses revealed enrichment of IL-1β regulatory pathways in RANK-positive endothelial cells, suggesting that RANK signaling promotes *Il1b* expression (Fig. 4e). Consistently, endothelial cells from middle-aged mice expressed higher *Il1b* levels than those from young mice (Fig. 4f, Extended Data Fig. 5b,c).

Immunofluorescence analysis further showed strong IL-1β signals in VE-cadherin-tom-positive endothelial cells and neighboring cells in middle-aged bone marrow, which were markedly reduced in EC-RANK cKO mice (Fig. 4g,h). Notably, CD31- and Emcn-positive endothelial cells lacked SPiDER-β-gal activity even in aged bone marrow (Extended Data Fig. 5d), indicating resistance to senescence. In vitro, rRANKL induced *Il1b* expression in RANK-overexpressing HUVECs, but not in bone marrow macrophages (Extended Data Fig. 5e,f).

Together, these findings indicate that endothelial RANK signaling promotes IL-1β production and bone marrow inflammaging in middle-aged mice.

Neutralization of IL-1β ameliorates age-associated phenotypes in bone marrow

To identify target cells of endothelial-derived IL-1β, we reanalyzed public scRNA-seq data from young (1.5-month-old; M1.5) and aged (16-month-old; M16) mice (GSE145477)[25]. UMAP visualization and violin plots showed high *Il1r1* expression in the *Cxcl12*$^{+}$*Lepr*$^{+}$ BMSC cluster in aged bone marrow (Fig. 5a,b; Extended Data Fig. 6a,b). DEG analysis revealed reduced osteoblast-related genes, including *Bglap* and *Col1a1*, in *Il1r1*-positive BMSCs (Extended Data Fig. 6c), suggesting that IL-1β–IL1R1 signaling impairs osteogenic differentiation. Consistently, IL-1β suppressed BMP2-induced alkaline phosphatase activity in ST2 cells (Extended Data Fig. 6d). scRNA-seq analysis further showed increased oxidative stress-response genes, including *Nfe2l2* and *Txnrd1*, in *Il1r1*-positive BMSCs (Extended Data Fig. 6e).

We therefore examined whether IL-1β induces senescence through oxidative stress. IL-1β increased γH2AX foci, ROS production, mitochondrial dysfunction, and *Ifnb* expression in ST2 cells, together with senescence markers including SA-β-gal, p16, and p21 (Fig. 5c,d; Extended Data Fig. 6f–i). These findings suggest that IL-1R signaling promotes mitochondrial dysfunction, ROS production, and cellular senescence in BMSCs.

To define the role of IL-1β in age-associated skeletal phenotypes, middle-aged mice were treated with anti–IL-1β antibodies. Neutralization of IL-1β reduced SPiDER-β-gal-positive BMSCs, rescued myeloid-biased hematopoiesis, and improved bone regeneration with increased Osx-positive osteoblasts (Fig. 5e–h). Together, these results demonstrate that IL-1β drives age-associated bone phenotypes, including BMSC senescence, myeloid-biased hematopoiesis, and impaired bone regeneration.

Effects of RANKL Ab on bone marrow senescence in middle-aged mice and diabetes mellitus patients

Finally, we investigated whether pharmacological blockade of RANKL could alleviate bone marrow aging. Anti-RANKL Ab treatment reduced the abundance of SPiDER-β-gal-positive senescent cells and rescued myeloid-biased hematopoiesis in middle-aged WT mice (Fig. 6a,b), supporting a central role for endothelial RANK signaling in age-associated bone marrow dysfunction.

Furthermore, GSEA of bulk RNA-seq data from iliac crest bone biopsies of postmenopausal women treated with placebo or denosumab (GSE141610) [26] revealed significant enrichment of the IL-1 response and inflammatory response gene sets in placebo-treated samples relative to denosumab-treated samples (Fig. 6c). The SenMayo gene signature also showed a modestly

227 enrichment in placebo-treated samples. These findings suggest that denosumab attenuates
228 inflammatory and senescence-associated transcriptional programs in human bone.
229 These findings suggest that the therapeutic effects of RANKL blockade may extend to age-
230 related diseases beyond osteoporosis. We therefore investigated whether denosumab improves
231 the diabetic phenotype in older adults with DM by evaluating changes in HbA1c levels.
232 Consistent with its established anti-resorptive effects, denosumab significantly increased BMD
233 in both groups. Notably, HbA1c levels were significantly reduced in patients with DM (6.87 ±
234 1.40% to 6.62 ± 1.32%; $P < 0.001$), whereas only a non-significant trend was observed in non-
235 DM individuals (5.58 ± 0.19% to 5.49 ± 0.21%; $P = 0.125$) (Fig. 6d). Together, these findings
236 raise the possibility that RANKL inhibition may provide benefits beyond skeletal protection,
237 including the amelioration of age-related metabolic dysfunction.
238 Collectively, our findings support a model in which age-associated activation of endothelial
239 RANK signaling drives skeletal inflammaging through IL-1β-dependent accumulation of
240 senescent cells and myeloid-biased hematopoiesis in the aged bone marrow (Fig. 6e).
241

Discussion

We demonstrate that increased RANK signaling in endothelial cells in the bone marrow of middle-aged mice drives bone inflammaging, which in turn induces myeloid-biased hematopoiesis and bone regeneration following myeloablation and bone marrow ablation, respectively. Our comprehensive analyses, including scRNA-seq and RNA-seq, revealed that RANKL-RANK signaling induces IL-1β expression in endothelial cells, and that IL-1β subsequently promotes cellular senescence in bone marrow cells including BMSCs. Furthermore, treatment with a RANKL antibody or an IL-1β antibody markedly ameliorates age-associated phenotypes in the bone marrow. Therefore, endothelial RANK signaling represents a potential therapeutic target for preventing the onset of bone marrow senescence.

Blood vessels, particularly Emcn^{high} CD31^{high} endothelial cells, have been shown to play important roles in bone development and hematopoiesis during aging[27, 28]. However, the mechanisms by which endothelial cells regulate bone mass and hematopoiesis remain incompletely understood. Recently, we demonstrated that endothelial RANK plays a critical role in recruiting monocyte-macrophage lineage cells, including osteoclast precursors, from the bloodstream into the bone marrow microenvironment in ovariectomy (OVX)-induced osteoporosis[29]. Blockade of endothelial RANKL-RANK signaling ameliorated OVX-induced bone loss without affecting bone mass under physiological conditions. In the present study, we further demonstrate a role for endothelial RANK in driving bone inflammaging in middle-aged

mice. We found that both the number and proportion of RANK-expressing endothelial cells, as well as the area occupied by RANKL-expressing cells, were increased in middle-aged bone marrow. These findings strongly suggest that endothelial RANK signaling substantially contributes to aging-associated phenotypes, including myeloid-biased hematopoiesis and impaired bone regeneration in middle-aged bone marrow.

The present study provides evidence that OPG protects bone and suppresses inflammaging in bone. Previous studies have reported that circulating OPG levels increase with age in both men and women[30,31]. However, these studies also demonstrated decreased bone mineral density and increased bone resorption markers, indicating that bone resorption is not primarily regulated by circulating OPG levels. Indeed, deletion of OPG in osteoblastic cells causes severe osteopenia without affecting serum OPG levels, further suggesting that local rather than systemic OPG is critical for bone homeostasis[32]. Therefore, serum OPG levels do not correlate with bone mass in either humans or mice. Taken together with our findings, these results suggest that age-associated increases in circulating OPG may preferentially act on vascular endothelial cells to suppress RANK signaling and subsequent inflammatory aging in the bone marrow.

Nearly half of endothelial cells express RANK in the middle-aged bone marrow, as shown in VE-cadherin-tom and RANK-tom reporter mice. Notably, genes associated with IL-1β production were enriched in these RANK-positive endothelial cells. These findings suggest that a subset of endothelial cells begins to express RANK and subsequently upregulates IL-1β in

response to RANKL stimulation. The molecular mechanisms underlying the increased number of RANK-expressing endothelial cells in middle-aged bone marrow remain unclear. A mouse brain capillary endothelial cell line, MBEC4, reportedly expresses Csf1r[33]. Csf1r signaling induces RANK expression in osteoclast-lineage cells[34], and Wnt5a-Ror2 signaling also promotes RANK expression in these cells[35]. These studies raise the possibility that Csf1r and Ror2 pathways could similarly promote RANK expression in endothelial cells. However, in our dataset, the expression levels of Csf1r and Ror2 were negligible in endothelial cell clusters (unpublished data), suggesting that these pathways are unlikely to contribute to RANK expression in middle-aged bone marrow endothelial cells. Further studies are required to clarify the mechanisms by which RANK expression becomes elevated in a subset of vascular endothelial cells during aging.

Our study proposes that IL-1β secreted from endothelial cells functions as an initiator of bone marrow inflammaging. IL-1β has been reported to induce cytosolic leakage of mitochondrial DNA (mtDNA) through NF-κB activation, thereby activating the cGAS-STING pathway and promoting the expression of SASP factors, including *Ifnb*[36]. In the present study, IL-1β treatment decreased mitochondrial membrane potential and induced Ifnb expression in ST2 cells. These findings indicate that IL-1β can drive SASP expression in cells that respond to IL-1 receptor signaling.

298 Our scRNA-seq reanalysis revealed that BMSCs express high levels of *Il1r1* mRNA,
299 encoding the IL-1β receptor. Consistent with this observation, IL-1β induced ROS production,
300 increased the DNA-damage marker γH2AX foci, and cellular senescence in stromal cell
301 cultures, suggesting that ROS production probably damages DNA. Notably, treatment with anti-
302 IL-1β antibodies markedly reduced SA-β-gal-positive senescent cells and partially rescued
303 myeloid-biased hematopoiesis in middle-aged mice. Thus, IL-1β represents a therapeutic target
304 for preventing the expansion of cellular senescence in middle-aged bone marrow.
305 NF-κB is well known as an inducer of IL-1β expression and as a key transcription factor
306 activated downstream of IL-1 signaling[37, 38]. RANKL-RANK signaling also activates NF-κB to
307 drive various biological processes, including osteoclastogenesis[39]. Notably, RANKL treatment
308 has been reported to induce *Il1b* mRNA and protein expression in rat neonatal cardiomyocytes
309 [40]. Based on these previous findings, it is highly plausible that RANK signaling activates NF-κB
310 and subsequently induces IL-1β expression in endothelial cells. Consistent with this hypothesis,
311 treatment with RANKL increased *Il1b* mRNA expression in human vascular endothelial cells
312 after ectopic expression of RANK. Furthermore, our analyses showed that the number of
313 RANKL-positive cells is also increased in middle-aged bone marrow. Together, these findings
314 suggest that bone marrow inflammaging may originate from enhanced RANK signaling in
315 endothelial cells, which in turn promotes IL-1β expression. Endothelial-derived IL-1β then acts

316 on bone marrow cells, including BMSCs, potentially establishing a vicious cycle of IL-1β
317 production that exacerbates inflammaging in middle-aged bone marrow.
318 Aged bone marrow macrophages are known to drive inflammaging not only within the bone
319 marrow but also in the liver, and they further contribute to impaired glucose metabolism[41]. In
320 our study, administration of RANKL antibodies markedly reduced senescent cells in the bone
321 marrow and rescued myeloid-biased hematopoiesis. Considering previous findings together
322 with our present results, it is plausible that treatment of DM patients with denosumab—a human
323 RANKL antibody—may suppress bone marrow inflammaging and consequently reduce
324 hemoglobin A1c levels, an indicator of long-term glucose control. In fact, serum HbA1c was
325 decreased in serum from patients administered RANKL antibody denosumab. We cannot
326 exclude the possibility that denosumab may also act directly on β cells to improve glucose
327 metabolism[42, 43]. Further studies are needed to determine whether the therapeutic effects of
328 denosumab in DM patients are mediated through the attenuation of inflammaging. Notably, the
329 findings presented here highlight the potential for extending denosumab treatment beyond
330 osteoporosis to broader anti-aging applications.
331

References

1. Palmer, A. K. et al. Cellular senescence: at the nexus between aging and diabetes. *Diabetologia* 62, 1835-1841 (2019). DOI: 10.1007/s00125-019-4934-x

2. Khosla, S. et al. The role of cellular senescence in aging and endocrine disease. Nat. Rev. *Endocrinol* 16, 263-275 (2020). DOI: 10.1038/s41574-020-0335-y

3. Ding Y. et al. Comprehensive human proteome profiles across a 50-year lifespan reveal aging trajectories and signatures. Cell 188, 5763-5784.e26 (2025). DOI: 10.1016/j.cell.2025.06.047.

4. Zhang, Q. et al. Senescent cells: an emerging target for diseases of aging. *Nat Rev Drug Discov* 16, 718-735 (2017). DOI: 10.1038/nrd.2017.116

5. Gasek, N. S. et al. Strategies for targeting senescent cells in human disease. *Nat Aging* 1, 870-879 (2021). DOI: 10.1038/s43587-021-00121-8

6. Rodier, F. et al. Persistent DNA damage signaling triggers senescence-associated inflammatory cytokine secretion. *Nat. Cell Biol*. 11, 973-979 (2009). DOI: 10.1038/ncb1909

7. Herranz, N. & Gil J. Mechanisms and functions of cellular senescence. *J Clin Invest.* 128, 1238-1246 (2018). DOI: 10.1172/JCI95148

8. Sogabe, Y. et al. Characterizing primary and secondary senescence in vivo. *Nat Aging* 5, 1568-1588 (2025). DOI: 10.1038/s43587-025-00917-y

9. Franceschi, C. et al. Inflammaging and ‘garb-aging’. *Trends Endocrinol Metab* 28, 199-212 (2017). DOI: 10.1016/j.tem.2016.09.005

10. Farr, J. et al. Targeting cellular senescence prevents age-related bone loss in mice. *Nat Med* 23, 1072-1079 (2017). DOI: 10.1038/nm.4385

11. Chaib, S. et al. Cellular senescence and senolytics: the path to the clinic. *Nat Med* 28, 1556-1568 (2022). DOI: 10.1038/s41591-022-01923-y

12. Ono T. et al. RANKL biology: bone metabolism, the immune system, and beyond. *Inflamm Regen* 40, 2 (2020). DOI: 10.1186/s41232-019-0111-3

13. Rao, S. et al. RANKL and RANK: From Mammalian Physiology to Cancer Treatment. *Trends Cell Biol* 28, 213-223 (2018). DOI: 10.1016/j.tcb.2017.11.001

14. Caiado, F. et al. IL-1 in aging and pathologies of hematopoietic stem cells. Blood 144, 368-377 (2024). DOI: 10.1182/blood.2023023105

15. Mitchell, C. A. et al. Stromal niche inflammation mediated by IL-1 signaling is a targetable driver of haematopoietic ageing. *Nat Cell Biol* 25, 30-41 (2023). DOI: 10.1038/s41556-022-01053-0

16. Frisch, B. J. et al. Aged marrow macrophages expand platelet-biased hematopoietic stem cells via Interleukin1B. *JCI Insight* 5, e124213 (2019). DOI: 10.1172/jci.insight.124213

17. Bucay, N. et al. osteoprotegerin-deficient mice develop early onset osteoporosis and arterial calcification. *Genes Dev* 12, 1260-8 (1998). DOI: 10.1101/gad.12.9.1260

18. Kim, Y. H. et al. Mid-old cells are a potential target for anti-aging interventions in the elderly. *Nat Commun* 14, 7619 (2023). DOI: 10.1038/s41467-023-43491-w

19. Young, K. et al. Decline in IGF1 in the bone marrow microenvironment initiates hematopoietic stem cell aging. *Cell Stem Cell* 28, 1473-1482.e7 (2021). DOI: 10.1016/j.stem.2021.03.017

20. Ho, Y. H. et al. Remodeling of bone marrow hematopoietic stem cell niches promotes myeloid cell expansion during premature or physiological aging. *Cell Stem Cell* 25, 407-418.e6 (2019). DOI: 10.1016/j.stem.2019.06.007

21. Elias, H. K. et al. Molecular mechanisms underlying lineage bias in aging hematopoiesis. *Semin Hematol* 54, 4-11 (2017). DOI: 10.1053/j.seminhematol.2016.11.002

22. Pang, W. W. et al. Human bone marrow hematopoietic stem cells are increased in frequency and myeloid-biased with age. *Proc Natl Acad Sci U S A* 108, 20012-7 (2011). DOI: 10.1073/pnas.1116110108

23. Mizoguchi T. et al. Identification of cell cycle-arrested quiescent osteoclast precursors in vivo. *J Cell Biol* 184, 541-554 (2009). DOI: 10.1083/jcb.200806139

24. Gibon, E. et al. Inflammation, aging, and bone regeneration. *J Orthop Translat* 10, 28-35 (2017). DOI: 10.1016/j.jot.2017.04.002

386 25. Zhong, L. et al. Single cell transcriptomics identifies a unique adipose lineage cell
387 population that regulates bone marrow environment. *Elife* 9, e54695 (2020). DOI:
388 10.7554/eLife.54695
389 26. Weivoda, M. M. et al. Identification of osteoclast-osteoblast coupling factors in humans
390 reveals links between bone and energy metabolism. *Nat. Commun*. 11, 87 (2020). Doi:
391 10.1038/s41467-019-14003-6
392 27. Kusumbe, A. et al. Coupling of angiogenesis and osteogenesis by a specific vessel subtype
393 in bone. *Nature* 507, 323-328 (2014). DOI: 10.1038/nature13145
394 28. Langen, U. et al. Cell-matrix signals specify bone endothelial cells during developmental
395 osteogenesis. *Nat Cell Biol* 19, 189-201 (2017). DOI: 10.1038/ncb3476
396 29. Kaneko, T. et al. The RANK/RANKL axis controls vascular dynamics in the bone marrow.
397 *Proc. Natl Acad. Sci. USA* 122, e2425366122 (2025). DOI: 10.1073/pnas.2425366122
398 30. Khosla, S. et al. Correlates of osteoprotegerin levels in women and men. *Osteoporos. Int.*
399 **13**, 394–399 (2002). DOI: 10.1007/s001980200045
400 31. Kudlacek, S. et al. Serum levels of osteoprotegerin increase with age in a healthy adult
401 population. *Bone* **32**, 681–686 (2003). DOI: 10.1016/S8756-3282(03)00129-1
402 32. Tsukasaki, M. et al. OPG Production Matters Where It Happened. *Cell Rep*.
403 2020;32(10):108124. DOI:10.1016/j.celrep.2020.108124

404 33. Jin, S. et al. Interleukin-34 restores blood-brain barrier integrity by upregulating tight
405 junction proteins in endothelial cells. *PLoS ONE* 9, e115981 (2014). DOI:
406 10.1371/journal.pone.0115981
407 34. Miyamoto, T. et al. Bifurcation of osteoclasts and dendritic cells from common progenitors.
408 *Blood* 98, 2544-2554 (2001). DOI: 10.1182/blood.V98.8.2544
409 35. Maeda, K. et al. Wn5a-Ror2 signaling between osteoblast-lineage cells and osteoclast
410 precursors enhances osteoclastogenesis. *Nat Med* 18, 405-412 (2012). DOI:
411 10.1038/nm.2653
412 36. Aarreberg, L. D. et al. Interleukin-1β Induces mtDNA Release to Activate Innate Immune
413 Signaling via cGAS-STING. *Mol Cell* 74, 801-815.e6. (2019). DOI:
414 10.1016/j.molcel.2019.02.038
415 37. Dinarello, C. A. Biologic basis for interleukin-1 in disease. *Blood* 87, 2095-2147 (1996).
416 DOI: 10.1182/blood.V87.6.2095.bloodjournal8762095
417 38. Dixit, V & Mak, T. W. NF-kappaB signaling. Many roads lead to madrid. *Cell* 111, 615-619
418 (2002). DOI: 10.1016/s0092-8674(02)01166-2
419 39. Boyce, B. F. & Xing, L. Functions of RANKL/RANK/OPG in bone modeling and
420 remodeling. *Arch Biochem Biophys* 473, 39-146 (2008). DOI: 10.1016/j.abb.2008.03.018
421 40. Ock, S. et al. Receptor activator of nuclear factor-κB ligand is a novel inducer of myocardial
422 inflammation. *Cardiovasc Res* 94, 105-114 (2012). DOI: 10.1093/cvr/cvs078

41. Hou, J. et al. Aged bone marrow macrophages drive systemic aging and age-related dysfunction via extracellular vesicle-mediated induction of paracrine senescence. *Nat Aging* 4, 1562-1581 (2024). DOI: 10.1038/s43587-024-00694-0

42. Kiechl, S. et al. Blockade of receptor activator of nuclear factor-κB (RANKL) signaling improves hepatic insulin resistance and prevents development of diabetes mellitus. *Nat Med* 19, 358-63 (2013). DOI: 10.1038/nm.3084

43. Kondegowda, N. G. et al. Osteoprotegerin and Denosumab Stimulate Human Beta Cell Proliferation through Inhibition of the Receptor Activator of NF-κB Ligand Pathway. *Cell Metab* 22, 77-85 (2015). DOI: 10.1016/j.cmet.2015.05.021

Methods

Experimental animals

OPG KO mice on a C57BL/6 background were purchased from CLEA Japan (Tokyo, Japan) as originally described (Mizuno et al., 1998)[44]. RANK-Cre mice were generated and maintained as previously described (Maeda et al., 2012)[35]. VE-cadherin-Cre (Kogata et al., 2006)[45] and RANK-flox mice (Powell et al., 2015)[46], as well as Rosa26-tdTomato mice (Madisen et al., 2010)[47], were obtained from the Jackson Laboratory. VE-cadherin-Cre mice were crossed with $RANK^{fl/fl}$ mice to generate EC-RANK cKO. VE-cadherin-Cre and RANK-Cre mice were crossed with Rosa26-tdTomato to generate lineage-tracing models. Unless otherwise stated, experiments were performed using male mice. For the bone marrow ablation experiments, female mice were used. The age of mice used in each experiment is indicated in the corresponding figure legends. All animals were maintained under specific pathogen-free (SPF) conditions at 24 ± 2 °C with 50–60% humidity under a 12-h light/dark cycle, with ad libitum access to sterilized water and chow. All animal experiments were approved by the Animal Management Committee of Matsumoto Dental University.

In vivo antibody and drug treatments

For RANKL neutralization, 8-week-old OPG KO mice or 32-week-old WT mice were injected subcutaneously with the neutralizing anti-RANKL monoclonal antibody OYC1

(Oriental Yeast; 5 mg/kg) or the non-neutralizing anti-RANKL control antibody OYC2 (Oriental Yeast; 5 mg/kg). Mice were euthanized 14 days after treatment[48].

For IL-1β neutralization, 32-week-old WT mice received six intravenous injections over 2 weeks of anti-IL-1β antibody (BE0246; InVivoMAb) or hamster control IgG (BE0260; InVivoMAb). For 5-fluorouracil (5-FU, 157027; Kyowa Kirin), 32-week-old control ($RANK^{fl/fl}$) and EC-RANK cKO mice, were injected intravenously with 5-FU (250 mg/kg) or saline. Survival was monitored for 20 days, and mice were euthanized at the endpoint[15, 23].

Microcomputed tomography (μCT)

Femora were harvested, soft tissues removed, and samples fixed in 4% paraformaldehyde (PFA, 162-16065; FUJIFILM). High-resolution μCT was performed using a ScanXmate-A080 system (Comscantecno). Images were reconstructed and trabecular bone parameters, including bone volume fraction (BV/TV), trabecular number (Tb.N), trabecular thickness (Tb.Th) and trabecular separation (Tb.Sp), were quantified using TRI/3D-BON software (Ratoc). Scanning conditions were 29 kV and 250 μA. A 1 mm region of the metaphyseal secondary spongiosa beginning 500 μm distal to the growth plate was analyzed[49].

Histology and immunofluorescence

For routine histological and immunofluorescence analyses, femora were fixed in 4% PFA at

4 ℃ overnight, followed by decalcification in 20% EDTA (041-22031; FUJIFILM) at 4 ℃ for 3 days. For p16 immunostaining, unfixed and undecalcified femora were used to preserve antigenicity. After the respective pretreatments, samples were cryoprotected in 20 % sucrose in PBS at 4 ℃ overnight, embedded in O.C.T. compound, and sectioned at 10–20 μm thickness using Kawamoto's film method with Cryofilm type IIIC (Section-Lab) and a tungsten carbide knife. Sections were blocked and incubated with primary antibodies overnight at 4 ℃, followed by incubation with appropriate secondary antibodies for 1 h at room temperature. Primary antibodies used included RANK/Tnfrsf11a (clone AF692; R&D Systems; 1:50), CD31/PECAM-1 Alexa Fluor 488 (clone FAB3628G; R&D Systems; 1:100), Endomucin (clone sc-65495; Santa Cruz Biotechnology; 1:50), Perilipin (clone D1D8; Cell Signaling Technology; 1:200), RANKL (rat polyclonal, sc-7628; Santa Cruz Biotechnology; 1:50), CDKN2A/p16^{INK4a} (clone EPR20418; Abcam; 1:50), F4/80 FITC (clone CI:A3-1; Abcam; 1:50), IL-1β (rabbit polyclonal, P420B; Invitrogen; 1:100), Ki67 FITC (clone SolA15; eBioscience; 1:100), Ly6G FITC (clone S19018G; BioLegend; 1:100), CD3 Alexa Fluor 488 (clone 17A2; BioLegend; 1:100), CD45R/B220 PE (clone RA3-682; BioLegend; 1:100), and anti-Sp7/Osterix (rabbit polyclonal, ab22552; Abcam; 1:200), LepR (goat polyclonal, AF497; R&D Systems; 1:100). Secondary antibodies included FITC-conjugated donkey anti-rat IgG (clone AP189F; Sigma-Aldrich; 1:200), Alexa Fluor 488 donkey anti-rabbit IgG (ab150073; Abcam; 1:500), Alexa Fluor 488 donkey anti-sheep IgG (ab150177; Abcam; 1:500), Alexa Fluor 594 donkey anti-

rabbit IgG (A21207; Invitrogen; 1:500), and Alexa Fluor 594 donkey anti-rat IgG (A21209; Invitrogen; 1:500). Control antibodies included purified rat IgG2b (clone 400601; BioLegend), normal rabbit IgG (148-09551; FUJIFILM), and sheep IgG (5-001-A; R&D Systems). Can Get Signal (NKB-601; TOYOBO) was used to enhance immunoreactions. Nuclei were counterstained with TO-PRO-3 iodide (T3605; Invitrogen). Senescence-associated β-galactosidase (SA-β-gal) activity was assessed using the SPiDER-β-gal (SG02; Dojindo) and SPiDER Blue (SG07; Dojindo) according to the manufacturer's instructions. Fluorescence images were acquired using a confocal laser scanning microscope (LSM 510; Carl Zeiss). For dynamic histomorphometric analyses, mice were injected intraperitoneally with calcein (Sigma-Aldrich; 20 mg/kg) twice at 72-h intervals, and femora were collected 24-h after the final injection. Samples were embedded in methyl methacrylate (MMA), sectioned at 5 μm thickness (SP1600; Leica), and mineral apposition rate (MAR), mineralizing surface per bone surface (MS/BS), and bone formation rate (BFR) were calculated[50]. MMA sections were stained with toluidine blue or TRAP/ALP (294-67001; Wako) for osteoblast and osteoclast quantification[49].

RANK$^+$ cell detection by Fluor555-rRANKL

Recombinant GST-RANKL (47187000; Oriental Yeast) was conjugated with HiLyte Fluor 555 using the HiLyte Fluor 555 Labeling Kit (LK14; Dojindo) according to the manufacturer's instructions[51]. Mice were injected intravenously with 0.7 mg/kg Fluor 555-rRANKL. 1 h later,

509 mice were perfusion-fixed with 4% PFA, femora collected, decalcified in 10% EDTA for
510 1 week, cryoprotected in 20% sucrose, and embedded in O.C.T. for sectioning (10 or 16 μm).
511
512 **Flow cytometry and cell sorting**
513 Bone marrow cells were flushed from femora and tibiae with complete medium (α-MEM
514 supplemented with 10% fetal bovine serum and L-glutamine). The cell suspension was
515 enzymatically digested with Dispase II (Oenon; 2 μg/mL), collagenase (FUJIFILM; 1 μg/mL),
516 and DNase I (Worthington; 10 μg/mL) at 37 °C for 30 min with gentle agitation. Cell
517 suspensions were filtered and subjected to red blood cell lysis using RBC lysis buffer (00-4333-
518 57; eBioscience). Cells were washed and stained with fluorochrome-conjugated antibodies
519 against CD31/PECAM1 Alexa Fluor 488 (clone FAB3628G; R&D Systems; 1:25), CD45 APC
520 (clone 30-F11; BioLegend; 1:100), Ly6G FITC (clone S19018G; BioLegend; 1:200), CD11b
521 Alexa Fluor 488 (clone M1/70; BioLegend; 1:100), CD3 Alexa Fluor 488 (clone 17A2;
522 BioLegend; 1:100), and mouse/human B220 PE (clone RA3-6B2; BioLegend; 1:100), mouse
523 Ter119 APC (clone TER-119; BioLegend; 1:100). Senescence-associated β-galactosidase
524 activity was detected by addition of SPiDER-β-gal reagent (Dojindo; 1:1000) before analysis.
525 After red blood cell lysis, bone marrow cells were incubated with CD45 MicroBeads (130-052-
526 301; Miltenyi Biotec) for magnetic separation. $CD45^+$ and $CD45^-$ fractions were isolated using
527 the MACS system, including a MACS MultiStand (130-042-303), MidiMACS Separator (130-

042-302), and LS Columns (130-042-401) (Miltenyi Biotec). The $CD45^-$ fraction was subsequently stained with fluorochrome-conjugated antibodies against mouse/rat CD31/PECAM1 Alexa Fluor 488 (clone FAB3628G; R&D Systems; 1:25), mouse CD45 APC (clone 30-F11; BioLegend; 1:100), and mouse Ter119 APC (clone TER-119; BioLegend; 1:100) and used for flow cytometric cell sorting. Cell populations were defined as $CD31^+CD45^-Ter119^-$ or $CD31^-CD45^-Ter119^-$ based on surface marker expression. Flow cytometry analysis was performed using an FC500 (Beckman Coulter). Flow cytometric cell sorting was performed using an FACSAria IIu (BD Biosciences). Data were analyzed using FlowJo software (BD Biosciences).

Quantitative real-time PCR

Tibiae were homogenized in TRIzol (Thermo Fisher) using a TissueLyser II (Qiagen). Total RNA was isolated using the NucleoSpin RNA kit (Macherey-Nagel), and cDNA synthesized using ReverTra Ace (TOYOBO). For endothelial and BMSC samples requiring preamplification, cDNA was generated using the iScript gDNA Clear cDNA Kit (Bio-Rad) followed by SsoAdvanced PreAmp Supermix. qPCR was performed using Fast SYBR Green Master Mix (Thermo Fisher) on a StepOnePlus system under standard cycling conditions. Relative expression was normalized to *Actb* (*ACTB*). Primer sequences are listed below.

Actb (mouse), 5′-CATCCGTAAAGACCTC-3′ (forward) and

5′-ATGGAGCCACCGATCCACA-3′ (reverse);

Cdkn1a (*p21*) (mouse), 5′-GCAGATCCACAGCGATATCCA-3′ (forward)

and 5′-AACAGGTCGGACATCACCAG-3′ (reverse);

Cdkn2a (*p16*) (mouse), 5′-TCTTTGTGTACCGCTGGGAAC-3′ (forward)

and 5′-GCATCGCTAGAAGTGAAGCTAAGAA-3′ (reverse);

Il1a (mouse), 5′-AGGGAGTCAACTCATTGGCG-3′ (forward)

and 5′-TGGCAGAACTGTAGTCTTCGT-3′ (reverse);

Il1b (mouse), 5′-GCAACTGTTCCTGAACTCAACT-3′ (forward)

and 5′-ATCTTTTGGGGTCCGTCAACT-3′ (reverse);

Il6 (mouse), 5′-CCACTTCACAAGTCGGAGGCTTA-3′ (forward)

and 5′-TGCAAGTGCATCATCGTTGTTC-3′ (reverse);

Tnfa (mouse), 5′-CTGTAGCCCACGTCGTAGC-3′ (forward)

and 5′-TTGAGATCCATGCCGTTG-3′ (reverse).

Ccl2 (mouse), 5′-GCTACAAGAGGATCACCAGCAG-3′ (forward)

and 5′-GTCTGGACCCATTCCTTCTTGG-3′ (reverse).

Cxcl1 (mouse), 5′-ACCGAAGTCATAGCCACACTC-3′ (forward)

and 5′-CTCCGTTACTTGGGGACACC-3′ (reverse);

Ifnb (mouse): 5′-GCCTTTGCCATCCAAGAGATGC-3′ (forward)

and 5′-ACACTGTCTGCTGGTGGA-3′ (reverse).

ACTB (human), 5′-CCAACCGCGAGAAGATGA-3′ (forward)
and 5′-CCAGAGGCGTACAGGGATAG-3′ (reverse);
IL1A (human), 5′-CGCCAATGACTCAGAGGAAGA-3′ (forward)
and 5′-AGGGCGTCATTCAGGATGAA-3′ (reverse);
IL1B (human), 5′-AGATGATAAGCCCACTCTACAG-3′ (forward)
and 5′-ACATTCAGCACAGGACTCTC-3′ (reverse);
IL6 (human), 5′-CAGGAGAAGATTCCAAAGAT-3′ (forward)
and 5′-CTCTTGTTACATGTCTCCTT-3′ (reverse);
TNF (human), 5′-CCCGAGTGACAAGCCTGTAG-3′ (forward)
and 5′-GATGGCAGAGAGGAGGTTGAC-3′ (reverse).
CCL2 (human), 5′-CAGCCAGATGCAATCAATGCC-3′ (forward)
and 5′-TGGAATCCTGAACCCACTTCT-3′ (reverse);
CXCL1 (human), 5′-AGGCAGGGGAATGTATGTGC-3′ (forward)
and 5′-AGCCCCTTTGTTCTAAGCCA-3′ (reverse);

Bone marrow ablation model

Performed as described by Matsushita et al. (2020)[52]. In 32-week-old female control and EC-RANK cKO mice, the knee joint was exposed and a 26G needle used to access the intercondylar space. Bone marrow was removed stepwise using K-files (#35-50). The cavity was irrigated

585 with saline and the incision sutured.

586

587 **Bulk RNA-sequencing**

588 Total RNA was extracted from mouse femurs as described above. RNA concentration and
589 integrity were assessed using a NanoDrop ONE spectrophotometer (Thermo Fisher Scientific)
590 and an Agilent TapeStation 4200 with the High Sensitivity RNA ScreenTape assay. For each
591 sample, 100 ng of total RNA was subjected to rRNA depletion using the NEBNext rRNA
592 Depletion Kit v2 (E7400; New England Biolabs), followed by library construction with the
593 NEBNext Ultra II Directional RNA Library Prep Kit for Illumina (E7760; New England
594 Biolabs). Indexed libraries were quantified using a Qubit Fluorometer and evaluated on a
595 TapeStation D1000 ScreenTape assay. Sequencing was performed on an Illumina NovaSeq 6000
596 platform using the S1 Reagent Kit v1.5, generating paired-end 50-bp reads. Raw BCL files were
597 converted to FASTQ format using bcl2fastq v2.20.0.422. Read quality was assessed with
598 FastQC. Adaptor trimming was performed using the Trim Reads v3.0 tool in CLC Genomics
599 Workbench v24.0.1 (Qiagen), with default parameters except that 1 bp at the 3′ end was
600 removed; reads < 36 bp were discarded. Trimmed reads were mapped to the Mus musculus
601 GRCm39 reference genome (Ensembl release 110) using strand-specific (reverse) settings
602 (similarity fraction 0.8; length fraction 0.8). Gene expression levels were quantified as
603 transcripts per million (TPM). Differential expression analysis was performed in R v4.5.1 using

Welch's t-test ($p < 0.05$). Genes with $|\log_2 \text{fold change}| \geqq 0.58$ were defined as differentially expressed. The top 30 differentially expressed genes, ranked by descending $\log_2$ fold change, were functionally annotated using UniProt. Annotation categories were ordered according to the number of assigned genes, and genes within each category were ranked by fold change. Venn diagrams were constructed to visualize upregulated and downregulated genes in Mcont compared with Ycont and McKO groups.

Single-cell RNA-seq data analysis

Publicly available single-cell RNA sequencing data (GSE145477)[25] were reanalyzed using R v4.4.1 and the Seurat package v4.3.0. Cells expressing fewer than 100 detected genes or more than 30% mitochondrial transcripts were excluded. Genes detected in fewer than three cells were removed. Remaining cells were normalized and scaled using the standard Seurat workflow. Highly variable genes (2,000 per dataset) were identified with the "vst" method. Principal component analysis (PCA) was performed, and datasets were integrated using reciprocal PCA (RPCA)-based anchoring (FindIntegrationAnchors and IntegrateData). Dimensionality reduction and clustering were performed using RunUMAP, FindNeighbors, and FindClusters. Clustering resolutions of 0.1 and 0.05 were used for Fig. 4d and Extended Data Fig. 5a, respectively. Endothelial cells with detectable *Tnfrsf11a* expression in the raw count matrix (count > 0) were defined as $RANK^+$ endothelial cells, whereas cells with no detectable

Tnfrsf11a expression (count = 0) were defined as $RANK^-$ endothelial cells. Differentially expressed genes were identified using the FindMarkers function in Seurat with the Wilcoxon rank-sum test. Genes with $p < 0.05$ and $|\log_2 \text{fold change}| \geqq 0.58$ were considered significant. Volcano plots were generated using ggplot2 and ggrepel. Gene set enrichment analysis (GSEA) was performed in Metascape (http://metascape.org) using the top 600 differentially expressed genes (ranked by $\log_2$ fold change), evaluating enrichment for Gene Ontology Biological Processes, KEGG pathways, and Reactome gene sets.

Cell cultures and cell staining

ST2 cells (RIKEN) were cultured in α-MEM supplemented with 10% FBS, L-glutamine, and antibiotic-antimycotic at 37 °C under 5% CO_2. Cells were treated with recombinant mouse IL-1β (R&D Systems; 5 ng/ml) for 10 days for senescence assays, which were assessed by SA-β-gal staining (KAA002RF; Millipore) and γH2AX immunostaining using an anti-phospho-Histone H2A.X antibody (clone 20E3; Cell Signaling Technology; 1:200). For osteogenic differentiation, ST2 cells were cultured in osteogenic medium consisting of 100 μg/mL L-ascorbic acid, 10 mM β-glycerophosphate, and 100 ng/ml recombinant human BMP2 (355-BEC-010; R&D Systems), with or without IL-1β. ALP staining was performed using a TRAP/ALP staining kit according to the manufacturer's instructions. HUVECs (C2519A; Lonza) were maintained in EGM-2 medium (CC-3162; Lonza). Cells were transiently

642 transfected with a TNFRSF11A (RANK) expression plasmid or control EGFP vector
643 (VectorBuilder) using the Cytofect™-HUVEC Transfection Kit (TF200K; Cell Applications)
644 according to the manufacturer's instructions. After 24 h, the medium was replaced with EBM-2,
645 and cells were stimulated with recombinant soluble RANKL (100 ng/mL) for 24 h. Total RNA
646 was extracted using TRIzol reagent for quantitative RT–PCR analysis. Mitochondrial membrane
647 potential was assessed using the JC-1 MitoMP Detection Kit (MT09; Dojindo) according to the
648 manufacturer's instructions. ST2 cells were treated with IL-1β (5 ng/mL) for 24 h and stained
649 with JC-1 for 1 h at 37 °C. Images were acquired using a Keyence fluorescence microscope.
650 ΔΨm was quantified in ImageJ as the background-corrected red/green fluorescence intensity
651 ratio on a per-cell basis (50 cells per experiment, $n = 3$). ST2 cells were treated with IL-1β (5
652 ng/ml) for 10 min. Intracellular reactive oxygen species (ROS) levels were measured using the
653 ROS Assay Kit -Photo-oxidation Resistant DCFH-DA- (R253; Dojindo) according to the
654 manufacturer's instructions, with staining performed for 30 min.
655
656 **Western blotting**
657 ST2 cells were treated with IL-1β (5 ng/ml) for 10 days and lysed in RIPA buffer
658 supplemented with protease and phosphatase inhibitors. Lysates were resolved by 10% SDS–
659 PAGE and transferred to PVDF membranes using a semi-dry system. Membranes were blocked
660 in 5% BSA in TBS-Tween (TBST) for 1 h at room temperature and incubated overnight at 4 °C

with primary antibodies against CDKN2A/p16^{INK4a} (clone EPR20418, Abcam, 1:1000), p21 (clone EPR18021; Abcam; 1:1000) and β-actin (8H10D10; Cell Signaling Technology; 1:5000). After washing, membranes were incubated for 1 h at room temperature with HRP-conjugated anti-rabbit secondary antibodies (NA934; Cytiva; 1:10000) for p16 and p21, and HRP-conjugated anti-mouse secondary antibodies (NA931; Cytiva; 1:50000) for β-actin. Signals were detected by enhanced chemiluminescence. Protein levels were normalized to β-actin and expressed relative to untreated controls.

Reanalysis of public RNA-seq data

Public RNA-seq count data (GSE141610) were downloaded from the Gene Expression Omnibus (GEO). Differential gene expression analysis was performed using the DESeq2 package. Genes were ranked according to the Wald statistic from the denosumab versus placebo comparison. Pre-ranked gene set enrichment analysis (GSEA) was performed using the GSEA function implemented in the clusterProfiler package. Gene sets were obtained from the Molecular Signatures Database (MSigDB) using the msigdbr package, including Hallmark (H), curated (C2), and Gene Ontology Biological Process (C5) collections. Gene sets containing 5–500 genes were included in the analysis, and multiple testing correction was performed using the Benjamini–Hochberg method.

Patients and Methods

This retrospective study analyzed 55 patients who received denosumab at Tokushima University Hospital between April 2014 and April 2016. The mean age of the subjects was 64.9 ± 3.5 years. The cohort included 41 patients with diabetes (12 males, 29 females) and 14 without diabetes (6 males, 8 females). All patients were diagnosed with primary osteoporosis according to Japanese diagnostic criteria[53]. Data on lumbar spine (L2-L4) bone mineral density (BMD) measured by dual-energy X-ray absorptiometry system (Horizon; Hologic) and HbA1c levels were extracted from medical records for the period before and 12 months after the administration of 60 mg denosumab.

To purely evaluate the effect of denosumab on glucose tolerance, the following patients were excluded:

1. Those treating with insulin.

2. Those receiving medications that affect glucose tolerance, such as glucocorticoids, testosterone, or psychotropic drugs.

3. Those who had changes in hypoglycemic medication or received nutritional counseling during denosumab treatment.

4. Patients with cancer.

For those patients who did not want to give consent to this study, we eliminated from the study. This study was approved by the Institutional Review Board of Tokushima University Hospital

699 (No. 3756-2).

700

701 **Quantification and statistical analysis**

702 Statistical analyses were performed using GraphPad Prism 9 (GraphPad Software). Data are
703 presented as mean ± s.d., and sample sizes are indicated in the corresponding figure legends.
704 Two-group comparisons were conducted using unpaired two-tailed Welch's t-tests. For
705 multiple-group comparisons, Brown–Forsythe and Welch ANOVA were performed, followed
706 by Dunnett's T3 multiple comparisons test. ImageJ was used to quantify $RANKL^+$ and ALP^+
707 areas, and fluorescence intensities were analyzed using ZEN 3.2 (Zeiss). A P value < 0.05 was
708 considered statistically significant. RNA-seq and scRNA-seq analyses are described separately.

709

710 **Reference**

711 44. Mizuno, A. et al. Severe osteoporosis in mice lacking osteoclastogenesis inhibitory
712 factor/osteoprotegerin. *Biochem. Biophys. Res. Commun.* 247, 610-615 (1998). DOI:
713 10.1006/bbrc.1998.8697

714 45. Kogata, N. et al. Cardiac ischemia activates vascular endothelial cadherin promoter in both
715 preexisting vascular cells and bone marrow cells involved in neovascularization. *Circ. Res.*
716 98, 897-904 (2006). DOI: 10.1161/01.RES.0000218193.51136.ad

717 46. Powell, J. J. et al. An endogenous nanomineral chaperones luminal antigen and
718 peptidoglycan to intestinal immune cells. *Nat. Nanotechnol.* 10, 361-9 (2015). DOI:
719 10.1038/nnano.2015.19

720 47. Madisen, L. et al. A robust and high-throughput Cre reporting and characterization system
721 for the whole mouse brain. *Nat. Neurosci.* 13, 133-40 (2010). DOI: 10.1038/nn.2467

722 48. Furuya, Y. et al. Increased bone mass in mice after single injection of anti-receptor activator
723 of nuclear factor-kappaB ligand-neutralizing antibody: evidence for bone anabolic effect of
724 parathyroid hormone in mice with few osteoclasts. *J. Biol. Chem.* 286, 37023-37031 (2011).
725 DOI: 10.1074/jbc.M111.246280

726 49. Bouxsein, M. L. et al. Guidelines for assessment of bone microstructure in rodents using
727 micro-computed tomography. *J. Bone Miner. Res.* 25, 1468-1486 (2010). DOI:
728 10.1002/jbmr.141

729 50. Parfitt, A. M. et al. Bone histomorphometry: Standardization of nomenclature, symbols, and
730 units. *J. Bone Miner. Res.* 2, 595-610 (1987). DOI: 10.1002/jbmr.5650020617
731 51. Kawakami, M. et al. Development of a method for the identification of receptor activator of
732 nuclear factor-κB^{+} populations in vivo. *J. Oral Biosci*. 63, 45–51 (2021). DOI:
733 10.1016/j.job.2021.01.009
734 52. Matsushita, Y. et al. A Wnt-mediated transformation of the bone marrow stromal cell
735 identity orchestrates skeletal regeneration. *Nat. Commun.* 11, 332 (2020). DOI:
736 10.1038/s41467-019-14029-w
737 53. Soen, S. et al. Diagnostic criteria for primary osteoporosis: year 2012 revision. *J. Bone*
738 *Miner. Metab.* 31, 247-57 (2013). DOI: 10.1007/s00774-013-0447-8
739

Acknowledgements

We thank the members of the Institute for Oral Science and the Department of Histology and Cell Biology, Matsumoto Dental University, for valuable discussions and technical assistance. We also thank the Department of Genomics & Proteomics, Advanced Science Research Center, Okayama University, for technical support in RNA-seq analysis, and the Research Center for Supports to Advanced Science, Shinshu University, for support with confocal microscopy and flow cytometric cell sorting.

Funding

This work was supported by JSPS KAKENHI grants 22K17008 (R.I.), 25K12979 (R.I.), 24H00653 (Y.K.), 22K18402 (Y.K.), and 24K02629 (N.U.) from the Ministry of Education, Culture, Sports, Science and Technology of Japan, and by grants from The Naito Foundation and the Terumo Life Science Foundation (Y.K.).

Author contributions

Y.K. initiated and supervised the project and wrote the manuscript. R.I. performed most of the experiments, analyzed data, prepared figures, and wrote the manuscript. T.T., M.I., Z.H., K.M., T.H. (Toru Hiraga), and H.Y. (Hisataka Yasuda) contributed to experiments and data analysis. T.H. (Tomoyo Hara), B.G., H.Y. (Hiroki Yamagami), and I.E. performed and analyzed

the clinical study. T.I., Y.A., and M.T. reanalyzed the scRNA-seq database. T.M. provided methodological support. M.N. and N.U. provided critical reagents and experimental animals. K.O., H.T., and N.U. contributed to study design and data interpretation. All authors reviewed and approved the final manuscript.

Competing interests

The authors declare no competing interests.

Data availability

The bulk RNA-seq data generated in this study will be deposited in the Gene Expression Omnibus (GEO) and will be publicly available upon publication. Publicly available scRNA-seq data analyzed in this study were obtained from GEO under accession number GSE145477.

Code availability

Scripts used for data analysis are available from the corresponding author upon reasonable request.

Materials & Correspondence

777 Correspondence and requests for materials should be addressed to Yasuhiro Kobayashi

778 (yasuhiro.kobayashi@mdu.ac.jp).

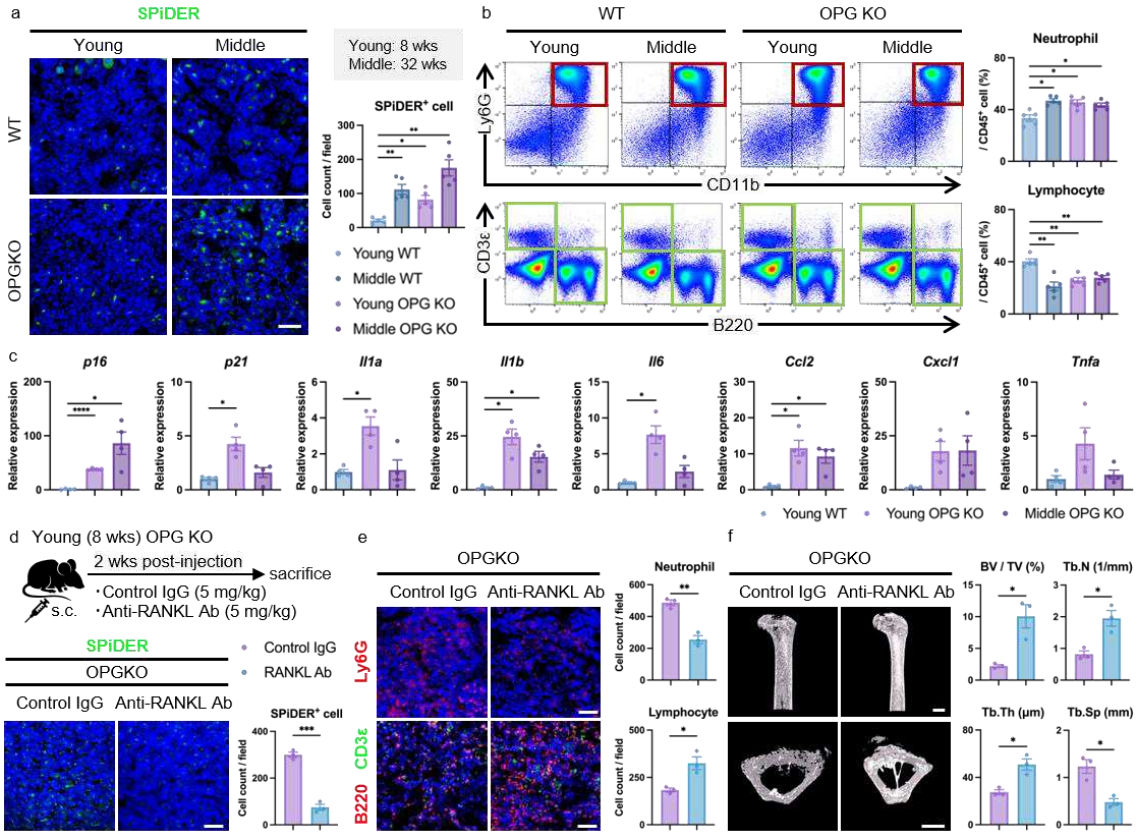


Figure 1 OPG deficiency accelerates age-associated bone phenotypes.

a, SPiDER-β-gal activity in femora from young and middle-aged WT and OPG KO mice. $n = 5$ biological replicates. Scale bar, 50 μm.

b, Flow cytometric analysis of $Ly6G^+CD11b^+$ neutrophils and $CD3^+$ or $B220^+$ lymphocytes within the $CD45^+$ bone marrow cell population from young and middle-aged WT and OPG KO mice. $n = 5$ biological replicates.

c, Quantitative RT–PCR analysis of senescence markers and SASP genes in tibiae from young and middle-aged WT and middle-aged OPG KO mice. $n = 4$ biological replicates.

d, SPiDER-β-gal activity in bone marrow from young OPG KO mice treated with anti-RANKL

antibody or control IgG. *n* = 3 biological replicates. Scale bar, 50 μm.

e, Immunofluorescence of $Ly6G^+$ neutrophils and $CD3^+$ or $B220^+$ lymphocytes in bone marrow from young OPG KO mice treated with anti-RANKL antibody or control IgG. *n* = 3 biological replicates. Scale bar, 50 μm.

f, μCT analysis of trabecular bone parameters in femora from young OPG KO mice treated with anti-RANKL antibody or control IgG. *n* = 3 biological replicates. Scale bar, 1 mm.

a–f, Data are presented as mean ± s.d. Statistical significance was determined using Brown–Forsythe and Welch ANOVA followed by Dunnett's T3 multiple-comparisons test or unpaired two-tailed Welch's *t*-test (*P < 0.05, **P < 0.01, ***P < 0.001, ****P < 0.0001).

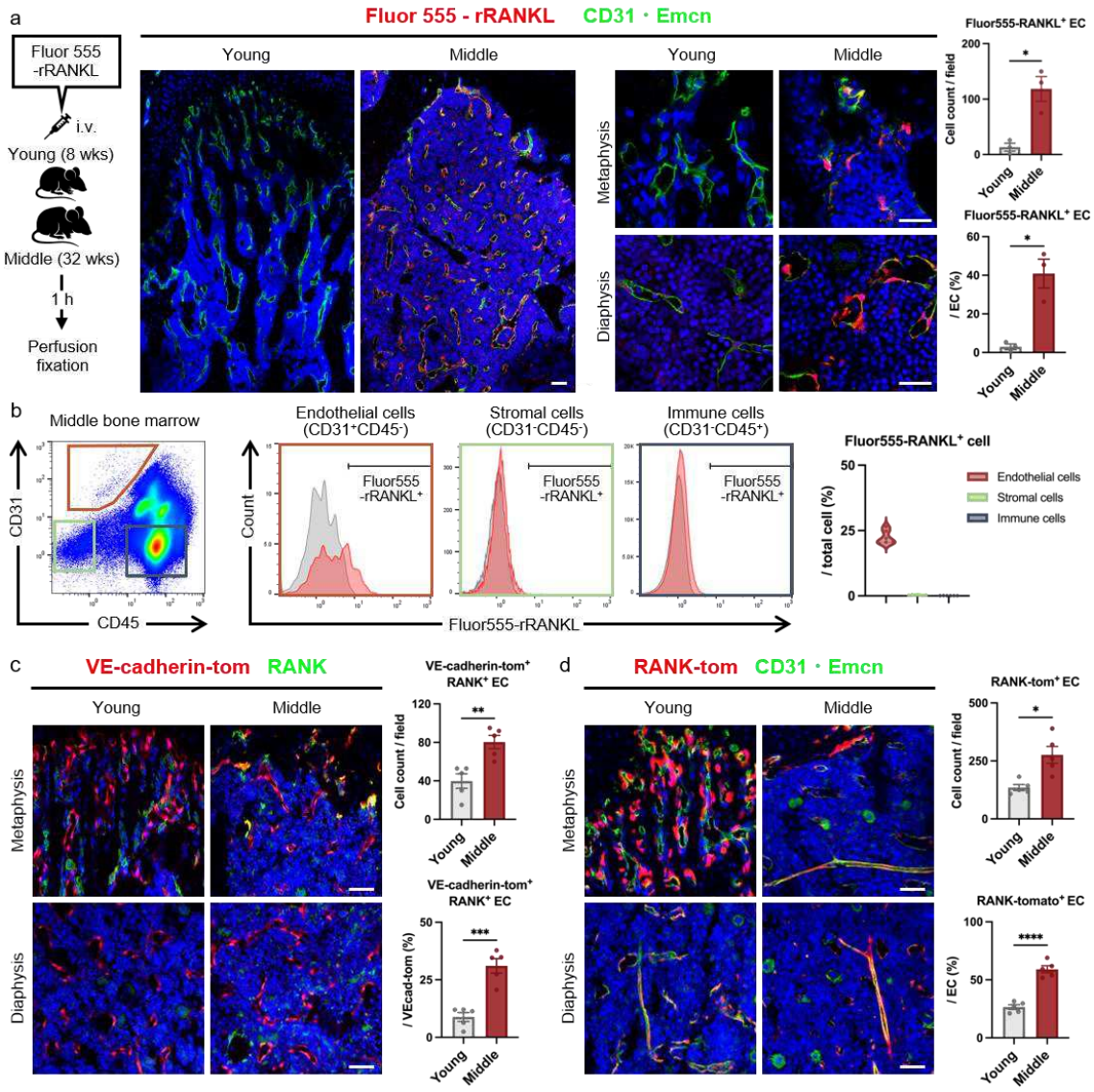


Figure 2 RANK⁺ endothelial cells are increased in middle-aged bone marrow

a, Immunofluorescence of CD31 and Emcn in femora from middle-aged control and EC-RANK cKO mice after intravenous injection of Fluor555-rRANKL. *n* = 3 biological replicates. Scale bar, 50 μm.

b, Flow cytometric analysis of Fluor555-rRANKL binding to endothelial ($CD31^+CD45^-$), stromal ($CD31^-CD45^-$), and immune ($CD31^-CD45^+$) cells populations in bone marrow from

middle-aged WT mice. Gray histograms indicate unstained controls, and pink histograms indicate Fluor555-rRANKL staining.

c, RANK immunofluorescence in femora from young and middle-aged VE-cadherin-tom mice. $n = 5$ biological replicates. Scale bar, 50 μm.

d, CD31 and Emcn immunofluorescence in femora from young and middle-aged RANK-tom mice. $n = 5$ biological replicates. Scale bar, 50 μm.

a,c,d, Data are presented as mean ± s.d. Statistical significance was determined using unpaired two-tailed Welch's *t*-test (*P < 0.05, **P < 0.01, ***P < 0.001, ****P < 0.0001).

b, Data are presented as median with interquartile range. Statistical significance was determined using the Kruskal–Wallis test (P < 0.0001).

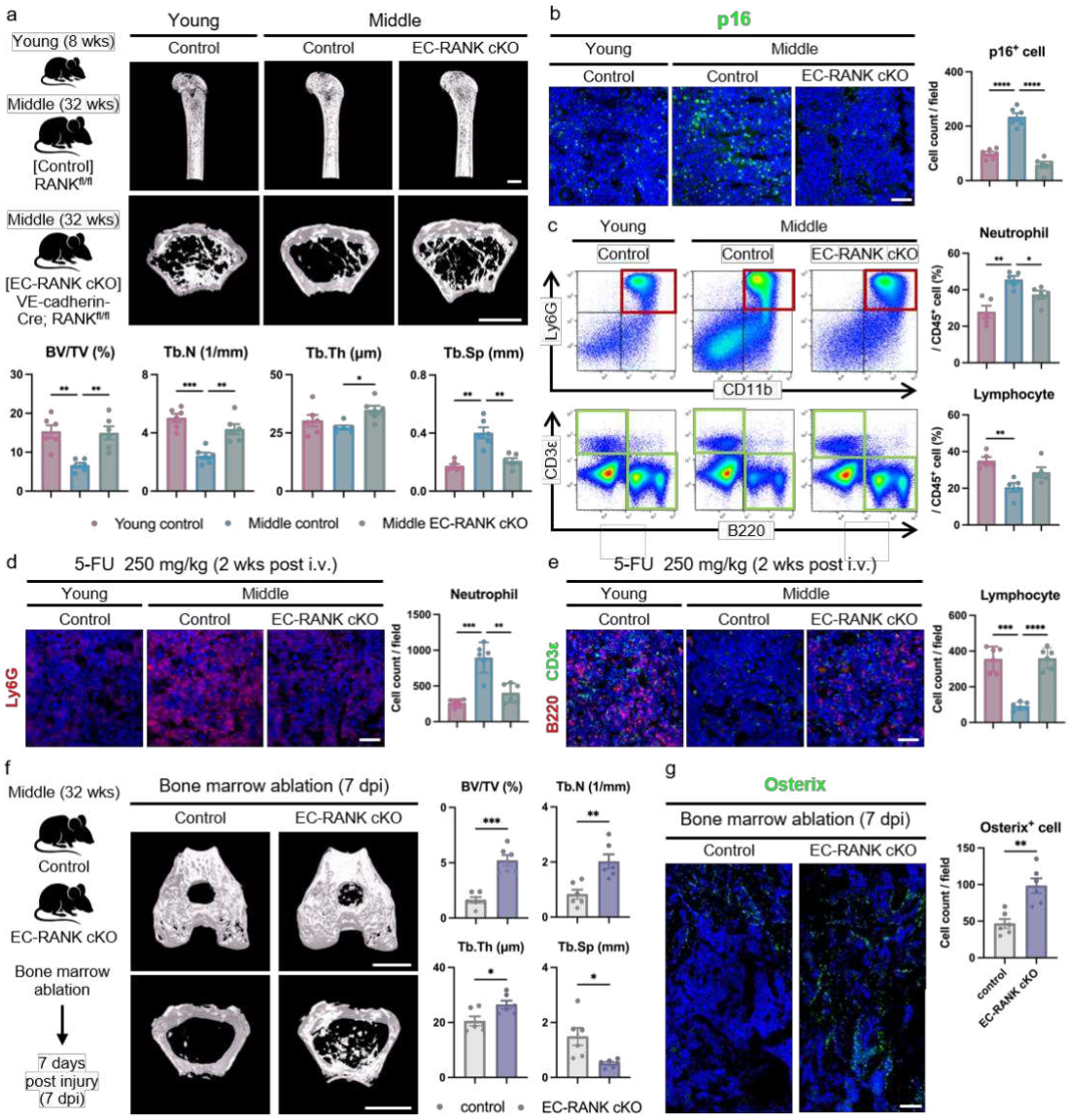


Figure 3 Endothelial RANK promotes age-associated bone phenotypes

a, μCT analysis of trabecular bone parameters in femora from young and middle-aged control ($RANK^{fl/fl}$) and middle-aged EC-RANK cKO (VE-cadherin-Cre; $RANK^{fl/fl}$) mice. $n = 6$ biological replicates. Scale bar, 1 mm.

b, p16 immunofluorescence in femora from young and middle-aged control and EC-RANK cKO mice. $n = 6$ biological replicates. Scale bar, 50 μm.

c, Flow cytometric analysis of $Ly6G^+CD11b^+$ neutrophils and $CD3^+$ or $B220^+$ lymphocytes within the $CD45^+$ bone marrow cell population from young and middle-aged control and EC-RANK cKO mice. $n = 5$ biological replicates.

d,e, Immunofluorescence of $Ly6G^+$ neutrophils (**d**) and $CD3^+$ or $B220^+$ lymphocytes (**e**) in bone marrow 2 weeks after 5-FU treatment in young and middle-aged control and EC-RANK cKO mice. $n = 6$ biological replicates. Scale bars, 50 μm.

f, μCT analysis of trabecular bone parameters in femora after bone marrow ablation from middle-aged control and EC-RANK cKO mice. $n = 6$ biological replicates. Scale bar, 1 mm.

g, Osterix immunofluorescence in femora after bone marrow ablation from middle-aged control and EC-RANK cKO mice. $n = 6$ biological replicates. Scale bar, 50 μm.

a–g, Data are presented as mean ± s.d. Statistical significance was determined using Brown–Forsythe and Welch ANOVA followed by Dunnett's T3 multiple-comparisons test or unpaired two-tailed Welch's *t*-test (*P < 0.05, **P < 0.01, ***P < 0.001, ****P < 0.0001).

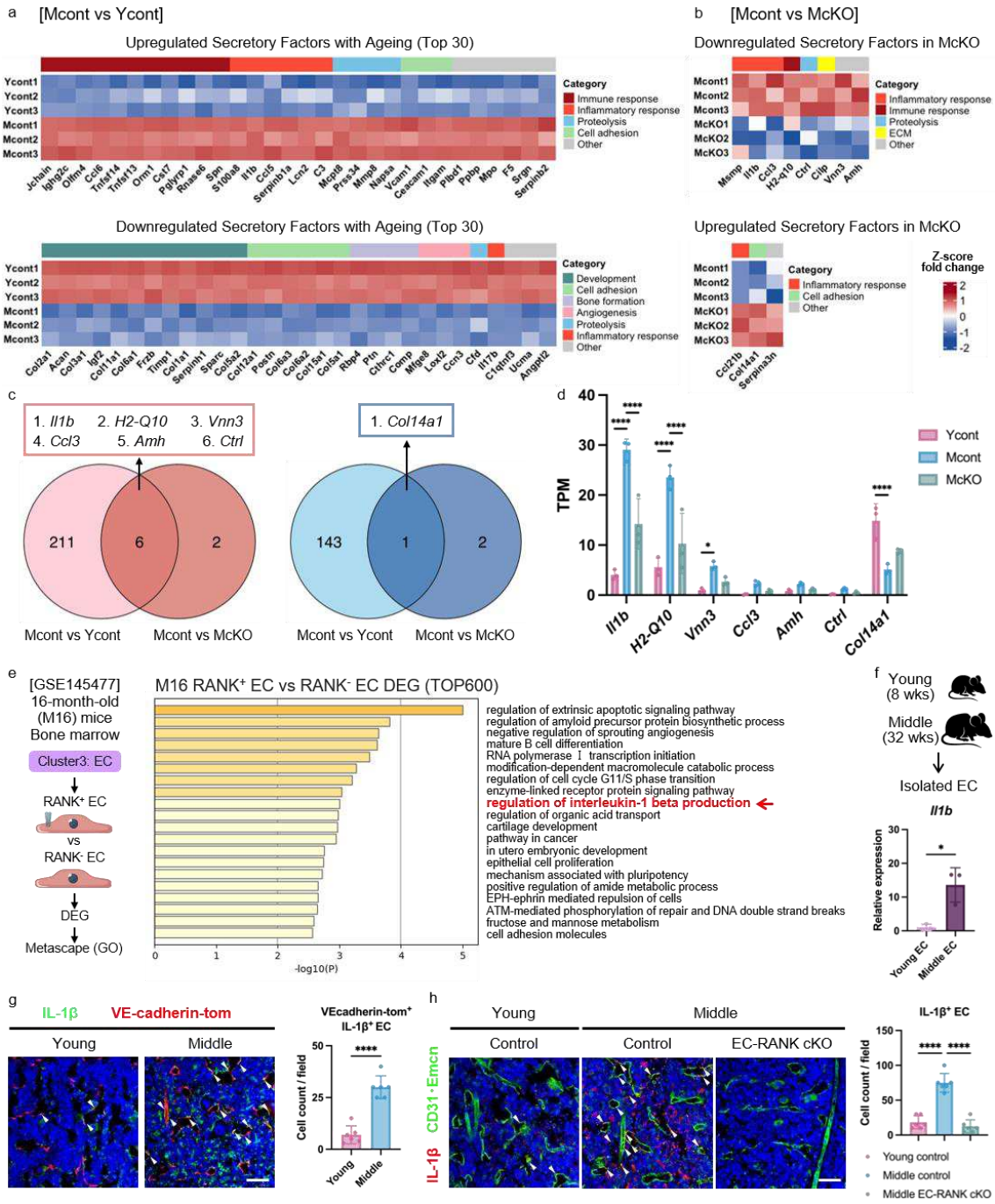


Figure 4 Aged endothelial cells express IL-1β in a RANK-dependent manner

a, Bulk RNA-seq analysis of femora from young control (Ycont), middle-aged control (Mcont), and middle-aged EC-RANK cKO (McKO) mice. Heatmap of secreted genes differentially expressed in Mcont compared with Ycont. *n* = 3 biological replicates.

b, Heatmap of secreted genes differentially expressed between Mcont and McKO mice. $n = 3$ biological replicates.

c, Venn diagrams of differentially expressed genes (DEGs; Welch's *t*-test, $P < 0.05$, $|\log_2 FC| \geqq 0.58$). Numbers indicate DEG counts and shared genes. $n = 3$ biological replicates.

d, TPM values of genes commonly upregulated or downregulated in Mcont compared with Ycont and McKO mice. $n = 3$ biological replicates.

e, Endothelial cells with detectable *Tnfrsf11a* transcripts in the raw count matrix (count > 0) were defined as $RANK^+$ endothelial cells, whereas cells with no detectable *Tnfrsf11a* transcripts (count = 0) were defined as $RANK^-$ endothelial cells.

f, Quantitative RT–PCR analysis of *Il1b* expression in endothelial cells ($CD31^+CD45^-Ter119^-$) isolated from tibiae and femora of young and middle-aged WT mice. $n = 3$ biological replicates.

g, IL-1β immunofluorescence in femora from young and middle-aged VE-cadherin-tom mice. $n = 6$ biological replicates. Scale bar, 50 μm.

h, IL-1β immunofluorescence in femora from young and middle-aged control and EC-RANK cKO mice. $n = 6$ biological replicates. Scale bar, 50 μm.

d,f–h, Data are presented as mean ± s.d. Statistical significance was determined using Brown–Forsythe and Welch ANOVA followed by Dunnett's T3 multiple-comparisons test or unpaired two-tailed Welch's *t*-test (*P < 0.05, ****P < 0.0001).

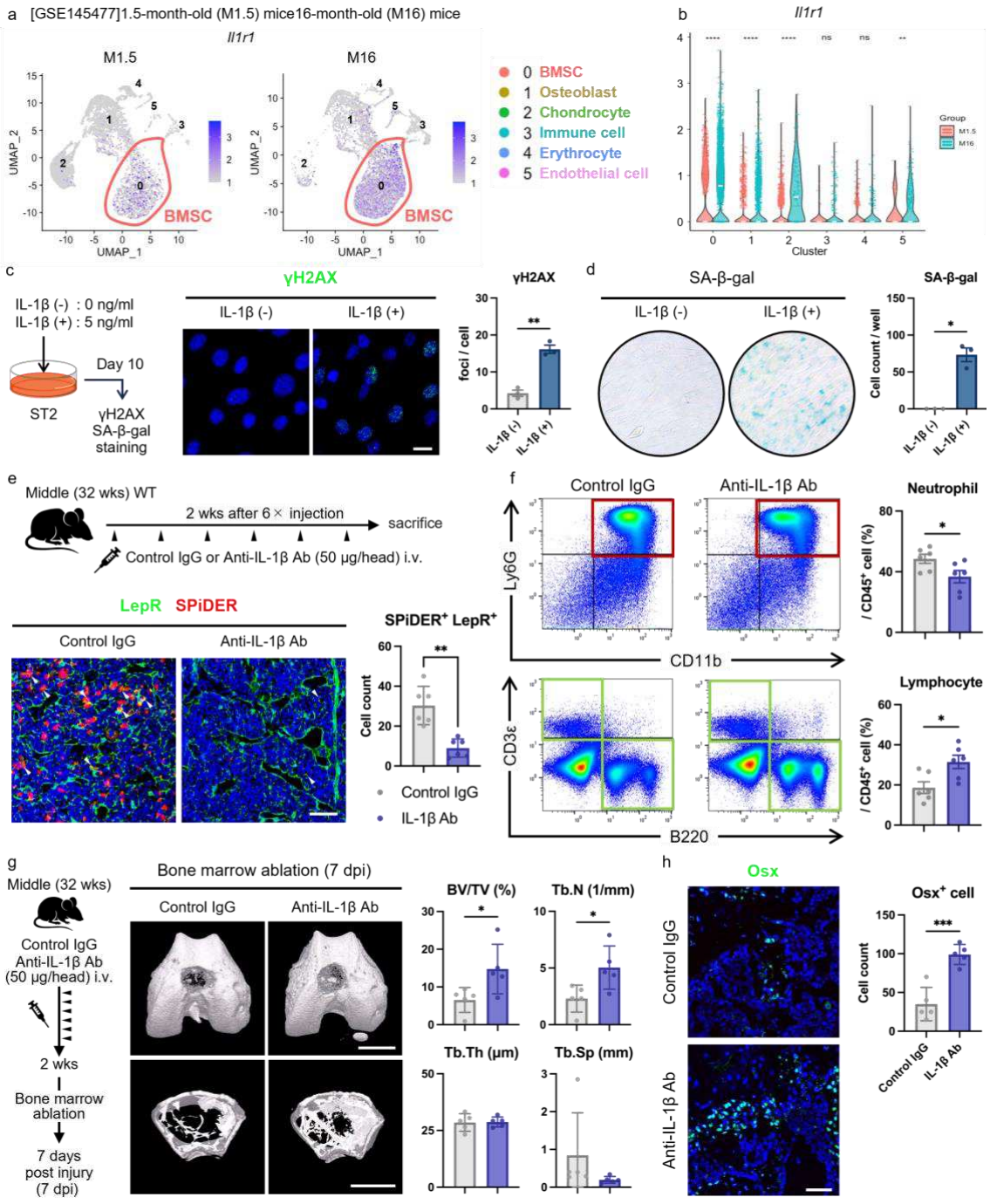


Figure 5 Neutralization of IL-1β ameliorates age-associated bone phenotypes

a,b, Feature (**a**) and violin (**b**) plots of *Il1r1* expression in bone marrow cells and BMSCs (cluster 0) at 1.5 and 16 months using scRNA-seq data (GSE145477). Statistical significance was determined using a two-sided Wilcoxon rank-sum test.

c, γH2AX immunofluorescence in ST2 cells treated with vehicle or IL-1β (5 ng/mL) for 10 days. *n* = 3 biological replicates.

d, SA-β-gal staining in ST2 cells treated with vehicle or IL-1β (5 ng/mL) for 10 days. *n* = 3 biological replicates.

e, LepR immunofluorescence and SPiDER-β-gal staining in femora from middle-aged WT mice treated with anti-IL-1β antibody or control IgG. *n* = 6 biological replicates. Scale bar, 50 μm.

f, Flow cytometric analysis of $Ly6G^+CD11b^+$ neutrophils and $CD3^+$ or $B220^+$ lymphocytes within the $CD45^+$ bone marrow cell population from middle-aged mice treated with anti-IL-1β antibody or control IgG. *n* = 6 biological replicates.

g,μCT analysis of trabecular bone parameters in femora after bone marrow ablation from middle-aged WT mice treated with anti-IL-1β antibody or control IgG. *n* = 5 biological replicates. Scale bar, 1 mm.

h, Osterix immunofluorescence in femora after bone marrow ablation from middle-aged WT mice treated with anti-IL-1β antibody or control IgG. *n* = 6 biological replicates. Scale bar, 50 μm.

c–h, Data are presented as mean ± s.d. Statistical significance was determined using unpaired two-tailed Welch's *t*-test (*P < 0.05, **P < 0.01).

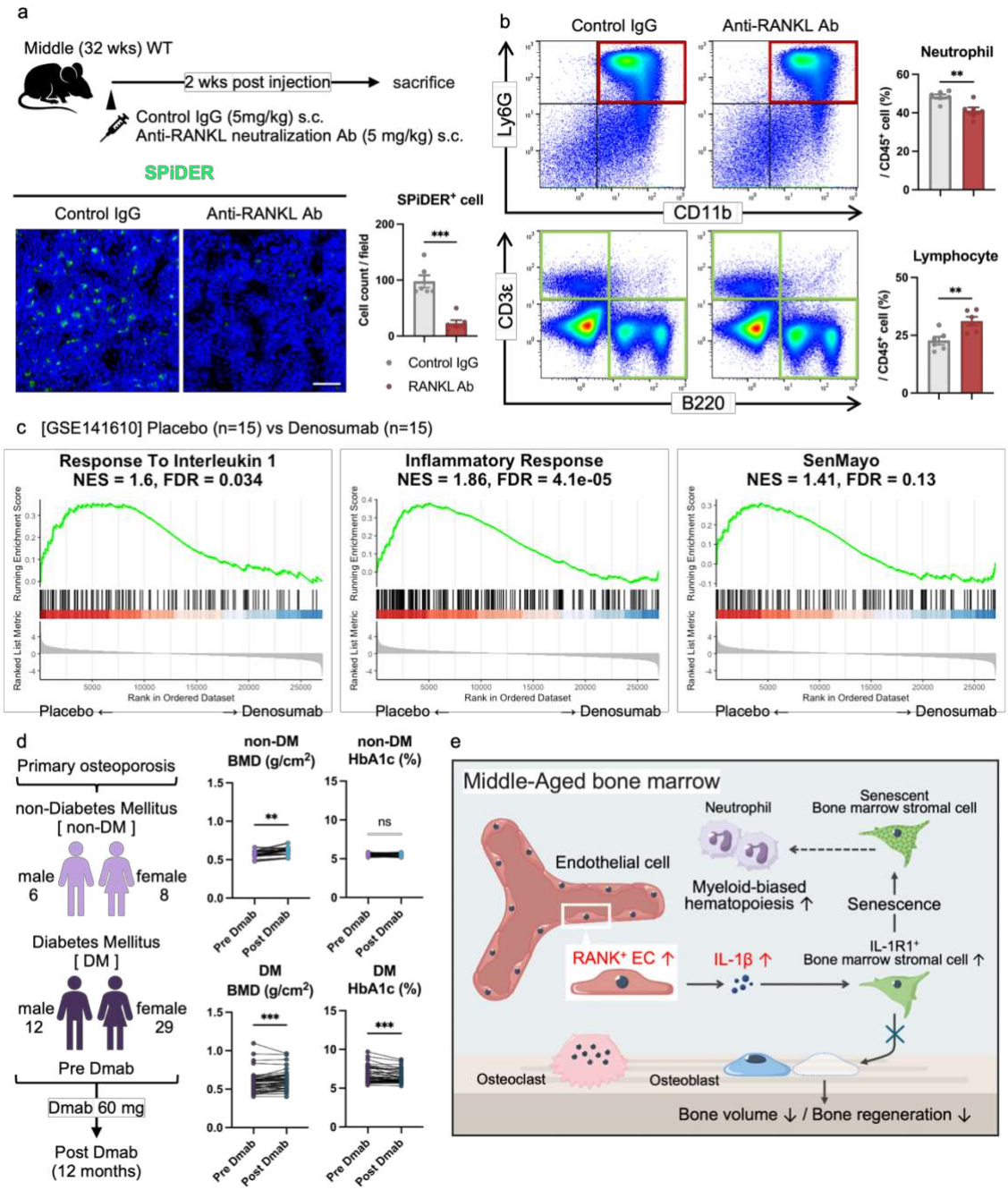


Figure 6 RANKL antibody ameliorates age-associated phenotypes in mice and humans

a, SPiDER-β-gal staining in bone marrow from middle-aged WT mice treated with anti-RANKL antibody or control IgG. $n = 6$ biological replicates. Scale bar, 50 μm.

b, Flow cytometric analysis of $Ly6G^+CD11b^+$ neutrophils and $CD3^+$ or $B220^+$ lymphocytes

within the $CD45^+$ bone marrow cell population from middle-aged mice treated with anti-RANKL antibody or control IgG. $n = 6$ biological replicates.

c, Gene set enrichment analysis (GSEA) of representative pathways associated with IL-1 signaling (GOBP_RESPONSE_TO_INTERLEUKIN_1), inflammation (HALLMARK_INFLAMMATORY_RESPONSE), and senescence (SAUL_SEN_MAYO) in denosumab- and placebo-treated human bone biopsies. Positive normalized enrichment scores (NES) indicate enrichment in the placebo group, whereas negative NES indicate enrichment in the denosumab group. NES and false discovery rate (FDR)-adjusted P values are shown for each pathway.

d, Study design and changes in bone mineral density (BMD) and serum HbA1c in non-diabetic (male, $n = 6$; female, $n = 8$) and diabetic (male, $n = 12$; female, $n = 29$) patients before and after denosumab (Dmab) treatment.

e, Proposed model of endothelial RANK signaling in skeletal inflammaging.

a–c, Data are presented as mean ± s.d. Statistical significance was determined using unpaired two-tailed Welch's *t*-test or paired two-tailed *t*-test (**P < 0.01, ***P < 0.001, ****P < 0.0001, ns, not significant).

Supplementary Files

This is a list of supplementary files associated with this preprint. Click to download.

- IwamotoetalExtendedDataFigureNatureAging.pdf